

This work was written as part of one of the author's official duties as an Employee of the United States Government and is therefore a work of the United States Government. In accordance with 17 U.S.C. 105, no copyright protection is available for such works under U.S. Law. Access to this work was provided by the University of Maryland, Baltimore County (UMBC) ScholarWorks@UMBC digital repository on the Maryland Shared Open Access (MD-SOAR) platform.

Please provide feedback

Please support the ScholarWorks@UMBC repository by emailing scholarworks-group@umbc.edu and telling us what having access to this work means to you and why it's important to you. Thank you.

JGR Space Physics

RESEARCH ARTICLE

10.1029/2020JA028518

Key Points:

- Mars thermospheric densities and composition are affected by this solar flare
- Thermospheric responses at fixed altitude (heating-based changes) and fixed number density (chemistry-based changes) differ
- The O/CO₂ ratio nearly triples at low number densities during this flare

Correspondence to:

A. G. Cramer,
agcramer@bu.edu

Citation:

Cramer, A. G., Withers, P., Elrod, M. K., Benna, M., & Mahaffy, P. R. (2020). Effects of the 10 September 2017 solar flare on the density and composition of the thermosphere of Mars. *Journal of Geophysical Research: Space Physics*, 125, e2020JA028518. <https://doi.org/10.1029/2020JA028518>

Received 23 JUL 2020

Accepted 26 SEP 2020

Accepted article online 10 OCT 2020

Effects of the 10 September 2017 Solar Flare on the Density and Composition of the Thermosphere of Mars

A. G. Cramer¹ , P. Withers^{1,2} , M. K. Elrod^{3,4} , M. Benna^{3,5} , and P. R. Mahaffy³ 

¹Astronomy Department, Boston University, Boston, MA, USA, ²Center for Space Physics, Boston University, Boston, MA, USA, ³NASA Goddard Space Flight Center, Greenbelt, MD, USA, ⁴CRESST, University of Maryland, College Park, MD, USA, ⁵CRESST, University of Maryland, Baltimore County, Baltimore, MD, USA

Abstract The effects of solar flares on the upper atmosphere of Mars are large but poorly constrained by observations. These effects are an important aspect of the response of Mars to space weather events and may also influence the escape of volatiles from Mars, particularly in the solar system's early history. Here we report the effects of the X8.2 flare on 10 September 2017 on the density and composition of the thermosphere of Mars. This analysis uses neutral number densities of He, O, N₂, CO, Ar, and CO₂ from the MAVEN Neutral Gas and Ion Mass Spectrometer (NGIMS). From these observations, we investigate how the enhanced solar irradiance during the flare produced changes in the neutral upper atmosphere of Mars due to atmospheric heating and photochemistry. Flare-produced photochemical changes in the neutral thermosphere of Mars have been previously implied but not quantified. We find that at fixed altitudes, the number densities of all species barring He increase and the O/CO₂ ratio decreases by ~15–45%, indicating thermal expansion. However, when viewed at fixed total number densities, the densities of CO₂ and Ar decrease, and the O/CO₂ ratio increases by up to a factor of ~3. The photodissociation of CO₂ is one photochemical process that produces changes resembling those identified. The quantified changes will help to constrain the shifting chemical makeup of the upper atmosphere due to these impactful flare events and may aid modeling of flare behavior and the impact of flares on the evolution of the Martian climate.

1. Introduction

1.1. The Thermosphere of Mars

The Martian thermosphere lies above the radiatively controlled mesosphere and below the collisionless, isothermal exosphere, ranging in altitude from approximately 100 to 250 km (Bougher, Roeten, et al., 2017). Its thermal structure is dominated by the absorption of ultraviolet and soft X-ray (SXR) solar photons and the subsequent conductive transport of this energy downwards to the higher-density mesosphere, from where it is radiated away to space (Chamberlain & Hunten, 1989).

The composition of the thermosphere varies with altitude due to molecular diffusion and photochemistry.

Molecular diffusion affects the thermosphere's composition because the majority of the thermosphere lies above the homopause, which varies between ~60 and 140 km (Slipski et al., 2018). Molecular diffusion in the thermosphere causes the physical process of diffusive separation, which separates elements and molecules (species) by mass. This tends to increase the relative abundances (mixing ratios) of light species with increasing altitude. Photochemistry affects the thermosphere's composition by causing the chemical process of photodissociation, which breaks up elements and molecules using the energy from the absorption of ultraviolet and SXR solar photons. This also tends to increase the relative abundances of light species.

Reflecting these characteristics, at lower altitudes, the thermospheric neutral composition is dominated by CO₂ molecules, the most abundant species in the Martian bulk atmosphere and most massive of the main neutral species in the upper atmosphere. At higher altitudes, the thermospheric neutral composition is dominated by atomic O, which is both lighter mass and highly chemically reactive. Neutral atomic oxygen is lost through reactions with many other atmospheric species and is continually replenished by CO₂ photodissociation. It is also generated by the dissociative recombination of O₂⁺, the most abundant ion species (Withers, 2009).

The chemical composition of the thermosphere can be characterized effectively by the O/CO₂ ratio.

The altitude-dependent composition of the thermosphere influences the environment of Mars in several distinct ways. The different neutral species present at thermospheric altitudes absorb solar radiation and conduct heat down to the mesopause with different rates and efficiencies, affecting the thermal structure of the upper atmosphere. In addition, the different photoionization cross sections of the neutral species affect rates of chemical reactions. Because a number of these chemical reactions involve ion species, the thermospheric composition also influences the structure of the ionosphere.

The neutral and plasma species affected by the chemical composition of the thermosphere make up the reservoir of upper atmospheric particles from which atmospheric escape occurs (Bougher, Pawlowski, et al., 2015; Jain et al., 2018).

As such, thermospheric composition affects the magnitude of the flux of volatiles escaping from Mars, as well as the net composition of that escape flux.

1.2. Effects of Solar Flares on the Thermosphere

Solar flares are impulsive outbursts of irradiance from the Sun (Schrijver & Siscoe, 2010). During a flare, the flux of solar photons at SXR, extreme ultraviolet (EUV), and far ultraviolet (FUV) wavelengths increases significantly over a period of minutes and then decreases exponentially to normal levels over the course of tens of minutes to several hours (Mendillo et al., 2006; Moore et al., 2014; Tsurutani et al., 2009). Such rapid and substantial changes in irradiance can significantly affect the thermosphere and associated aspects of the environment of Mars. Heating, photoionization, and photodissociation rates will increase, which should lead to thermal expansion of the upper atmosphere, greater plasma densities in the ionosphere, and greater production of neutral atomic oxygen, respectively (Elrod et al., 2018; Gurnett et al., 2005; Mendillo et al., 2006; Thiemann et al., 2018).

The effects of solar flares on the thermosphere of Mars are important to characterize. They illustrate the behavior of the Mars atmospheric system under extreme conditions and how the system responds to an impulsive event. Characterization of these solar flare effects will provide insight into how the Mars environment evolved early in the history of the solar system, when flares were much more common (Curry et al., 2019; Jain et al., 2018; Lillis et al., 2015). If changes in ionospheric and thermospheric conditions during a solar flare significantly enhance the loss rate and composition of escaping volatiles, the infrequent and brief, yet intense, solar flares may additionally influence today's time-averaged escape rate.

Yet due to the infrequent occurrence and short duration of solar flares, few observational constraints on the behavior of the Mars environment in the presence of a solar flare are available.

The first observations of flare effects at Mars reported the enhancement of ionospheric electron densities during solar flares (Fallows et al., 2015; Gurnett et al., 2005; Mendillo et al., 2006). These studies found that densities increase more for larger magnitude flares, as expected, and that densities increase more at low altitudes, consistent with the hardening of the solar spectrum during a flare (Kong et al., 2013).

The first observations of flare effects on the neutral thermosphere of Mars were reported by Thiemann et al. (2015). They analyzed Ar number density measurements collected by the MAVEN spacecraft at the times of 14 solar flares and found rapid and short-lived heating of the thermosphere during the flares.

The first observations of flare effects on the composition of the thermosphere and ionosphere of Mars occurred in September 2017, when MAVEN observations captured the effects of an X8.2 solar flare (Elrod et al., 2018; Thiemann et al., 2018).

In the thermosphere, Elrod et al. (2018) reported that densities of CO₂, Ar, N₂, CO, and O were enhanced by factors as large as 2.5–5 during the flare. The relative changes in species number densities were greater with increasing altitude and more pronounced for species of larger mean molecular mass. Elrod et al. (2018) also noted that the O/CO₂ ratio decreased at fixed altitudes and calculated an increase in the temperatures of all major neutral species by ~100 K during the flare. From these observations, Elrod et al. (2018) concluded that flare heating leads to thermal expansion, which inflates the thermosphere to raise the densities and temperatures of species.

In the ionosphere, Thiemann et al. (2018) reported that the densities of individual ion species O^+ , O_2^+ , and CO_2^+ also increased during the flare. Ion densities increased by as much as 100% from their baseline values. A different picture was obtained when these observations were viewed at fixed neutral pressure levels rather than fixed altitudes. The densities of O_2^+ and CO_2^+ decreased during the flare at neutral pressures less than 10^{-7} Pa (high altitudes) and had no significant change from their typical densities at higher neutral pressure levels (lower altitudes). Thiemann et al. (2018) also noted that the O/CO_2 ratio, which Elrod et al. (2018) reported to decrease at fixed altitudes, increased when viewed at fixed neutral pressure levels. Thiemann et al. (2018) interpreted these contrasting observations in the fixed pressure reference frame as showing that the thermosphere and ionosphere were elevated at the time of the observation due to thermal expansion but that the observed composition changes were primarily caused by photochemical processes. This would explain the increase in the density of O^+ (derived from the photoionization of O) and the decreases in the densities of CO_2^+ (derived from the photoionization of CO_2) and O_2^+ (derived from a charge exchange reaction involving CO_2^+), which were each observed at fixed pressure levels.

During the same solar flare on 10 September 2017, a “significant enhancement in H escape flux was observed for the first time at Mars on such a relatively short timescale (few days)”, demonstrating the enhancement of atmospheric loss rates stemming from flare-produced upper atmosphere changes at Mars (Mayyasi et al., 2018).

1.3. Aim

The earlier works discussed above have shown that solar flares can have significant effects on the thermosphere, ionosphere, and escape fluxes at Mars. It is clear that flares affect the thermosphere by causing thermal expansion and changes in chemical composition. However, the relative significance of these two factors has not yet been established.

In order to advance understanding of their relative significance, the aim of this work is to characterize how (1) densities of thermospheric species and (2) thermospheric composition, particularly the O/CO_2 ratio, changed due to these two processes during the solar flare that impacted Mars on 10 September 2017.

The structure of this article is as follows. Section 2 discusses the September 2017 solar storms and their effects in the inner solar system. Section 3 describes the thermosphere densities data set used in this article. Section 4 assesses the effects of this flare on the total number density of the thermosphere. Section 5 assesses the effects of this flare on the number densities of individual species in the thermosphere. Section 6 assesses the effects of this flare on the chemical composition of the thermosphere. Section 7 assesses the effects of this flare on the O/CO_2 ratio in the thermosphere. Section 8 assesses the influence of this flare in the context of other significant thermosphere disturbances. Section 9 discusses the results of the preceding sections. Section 10 presents the conclusions of this work.

2. Solar Storms of September 2017 and Their Effects at Earth and Mars

A series of intense solar storms in September 2017 launched a succession of solar flares, coronal mass ejections (CMEs), and solar energetic particles (SEPs) into the heliosphere (Bruno et al., 2019; Chamberlin et al., 2018; Jiggins et al., 2019; C. O. Lee, Jakosky, et al., 2018; Luhmann et al., 2018).

During the week of 4 to 10 September 2017, the Sun emitted multiple M- and X-class flares, including “X9.3 (6 September) and X8.2 (10 September) flares, the largest flares that have occurred during Solar Cycle 24” (Chamberlin et al., 2018). These large flares were accompanied by fast-moving CMEs ($>1,000$ km s $^{-1}$), which produced shocks that accelerated strong fluxes of SEPs (Luhmann et al., 2018).

These solar events and their effects in the inner heliosphere were charted by observing platforms such as GOES, SDO, TIMED, ACE, and SOHO (near Earth), LRO (at the Moon), MAVEN, Curiosity, and Mars Express (at Mars), and by the sole active STEREO spacecraft, STEREO-A (at 1 AU) (Chamberlin et al., 2018; C. O. Lee, Jakosky, et al., 2018; Luhmann et al., 2018). The orbital spacing of Earth from Mars (at superior conjunction) and STEREO-A (at an intermediate heliocentric longitude) provided well-distributed coverage of observations (C. O. Lee, Jakosky, et al., 2018; Luhmann et al., 2018). The instruments at these positions identified substantial particle, photon, and magnetospheric changes to the surrounding interplanetary and planetary environments.

At Earth, the solar activity of these September 2017 storms affected the geospace environment significantly. Earth's plasmasphere was severely eroded (Obana et al., 2019), and at lower altitudes, a CME shock increased the outflow flux of O^+ from the ionosphere to three times a baseline value already elevated by the earlier impacts of X-class flares and another shock (Schillings et al., 2018). The CMEs and their associated SEPs corresponded to decreased intensities of cosmic rays (Forbush decreases) as the changing interplanetary magnetic field deflected a greater proportion away from Earth (Badriddin et al., 2019; Chertok et al., 2018). However, the intensities of high-energy charged particles at Earth's surface increased (ground level enhancements), as the enhanced fluxes of SEPs augmented the typical background provided by cosmic rays (Cohen & Mewaldt, 2018; Copeland et al., 2018; Matthiä et al., 2018; Mavromichalaki et al., 2018; Mishev & Usoskin, 2018).

The intense solar effects at Earth impacted critical technological systems. The performance of GPS and similar navigation systems were degraded by enhanced solar radio noise at the GPS frequencies and by temporal variations in ionospheric total electron content (Berdermann et al., 2018; Linty et al., 2018; Obana et al., 2019). In addition, high-frequency (3–30 MHz) radio communications, which rely upon reflections from the ionosphere to propagate beyond the horizon, were disrupted due to the perturbed state of the ionosphere (Aa et al., 2019; Bland et al., 2018; Chakraborty et al., 2019; Curto et al., 2018; Yamauchi et al., 2018; Yasyukevich et al., 2018). This disruption of communications was particularly severe in the Gulf of Mexico and Caribbean regions, where it affected recovery from multiple hurricanes and earthquakes (Frissell et al., 2019; Gonzalez-Esparza et al., 2018; Redmon et al., 2018). A number of additional geospace effects with notable potential to produce significant impacts on technological systems were also observed at Earth during this period. For instance, rapid changes in the terrestrial magnetic field environment caused strong geomagnetically induced currents, a phenomenon that can damage critical technological infrastructures that contain ground-based conducting systems, such as power grids, railways, telecommunication cables, and oil and gas pipelines (Clilverd et al., 2018; Dimmock et al., 2019; Piersanti et al., 2019). The SEPs, which were identified to enter the magnetosphere, likewise increased the likelihood of failures in spacecraft electronics (O'Brien et al., 2018), and on the International Space Station, the Moon, and Mars, increased radiation doses were observed (Berger et al., 2018; Hassler et al., 2018; Schwadron et al., 2018).

Effects of the solar storms on Mars and its surrounding space environment were also significant. The September 2017 event produced the largest SEP event seen by MAVEN since its arrival at Mars in 2014 and the fourth largest seen by Mars Express since its arrival at Mars in 2004 (Ramstad et al., 2018). SEPs significantly enhanced nightside ionosphere densities, producing peak electron densities of $1\text{--}2 \times 10^4 \text{ cm}^{-3}$ around 120 km altitude (Harada et al., 2018). Bright aurorae were also detected across the entire observable nightside of Mars and originated at a low altitude of 60 km, indicating production by particle precipitation at unusually high energies. The aurorae were 25 times brighter than previously observed diffuse aurorae at Mars and left localized patches of emissions in regions of open magnetic field lines as the event diminished (Schneider et al., 2018).

At the surface of Mars, the radiation dose doubled for almost a day, before falling below pre-event levels due to a Forbush decrease. The flux of high-energy charged particles ($<100 \text{ MeV}$ protons) increased by an order of magnitude more than did the radiation dose (Ehresmann et al., 2018; Zeitlin et al., 2018).

The X8.2 class solar flare, which impacted Mars on 10 September 2017, increased ionospheric electron densities and decreased electron temperatures across all fixed thermosphere altitudes. Since no changes in these quantities were present when viewed at fixed pressure levels, these effects were consistent with an overall expansion of the neutral atmosphere within which the ionosphere is embedded. The energy spectrum of photoelectrons in the ionosphere of Mars also showed appreciable increases in the 20–500 eV range and included the Auger peaks of oxygen and carbon (Xu, Thiemann, et al., 2018).

By contrast, the atmospheric composition of ions at fixed pressure levels did change: the O_2^+ and CO_2^+ densities decreased. This behavior was interpreted as being caused by the observed increase in the neutral O/CO_2 ratio at fixed pressure levels (Thiemann et al., 2018).

During the period of enhanced electron and ion densities in the Martian atmosphere, upward plasma drifts likely occurred, leading to enhanced plasma escape rates (Mendillo et al., 2018). The movement of magnetospheric boundaries inwards due to the solar storm-affected interaction between Mars and the solar wind

likely also contributed to ion escape rates, as the boundary between draped and closed magnetic field regions descended down to ionospheric altitudes and the area of open field lines increased (Ma et al., 2018; Xu, Fang, et al., 2018).

Heating of the neutral upper atmosphere likewise caused an enhancement to atmospheric escape rates, with a fivefold increase in hydrogen escape rates and a 20% increase in the oxygen escape rate due to the expansion of the hot oxygen corona (Jain et al., 2018; Y. Lee, Dong, et al., 2018; Mayyasi et al., 2018). The densities of all neutral species above 200 km were increased because of the effects of the 10 September 2017 flare, due in part to the thermal expansion of the atmosphere and in part to compositional changes occurring at fixed pressure levels, which potentially stemmed from photochemistry. Changes to the neutral species densities affected the density and compositional changes of ion species (Thiemann et al., 2018), further demonstrating the significance of determining changes to the neutral O/CO₂ ratio during the flare event.

3. Data

In situ measurements of number densities (cm⁻³) of neutral species in the upper atmosphere of Mars are available from the MAVEN Neutral Gas and Ion Mass Spectrometer (NGIMS) instrument (Mahaffy, Benna, Elrod, et al., 2015; Mahaffy, Benna, King, et al., 2015). NGIMS data are acquired between periapsis altitude (~150 km) and an upper boundary set by instrument sensitivity. The upper boundary for reported densities varies by species but is in the approximate range of 240–300 km. Individual measurements are taken every 2 s during a 20 min collection period for each periapsis pass (every 4.5 hr). We use the MAVEN NGIMS Level 2 (Version 08, Revision 01) densities from the inbound portion of orbits only, as out-bound neutral density measurements of O, a critical species, are unreliable due to interactions between this species and the instrument walls (Benna & Elrod, 2016; Liu et al., 2018). As is discussed in detail in section 5.1, we divide reported CO number densities by a factor of 4.

Here we consider data from MAVEN Orbits 5715–5720 (10–11 September 2017). NGIMS number density measurements on MAVEN Orbit 5718 were acquired approximately 90 min after the peak of the flare event, at a periapsis time of ~17:42 UTC on 10 September 2017 (Fang et al., 2019). At the time of these observations, the EUV flux had decreased to 25% of its peak value during the flare (Elrod et al., 2018). Consistent with earlier work, we find that thermospheric responses to flare effects were present solely during this one orbit. Therefore, we combine measurements from the five surrounding orbits to generate a single representation of baseline atmospheric conditions. Observations from Orbit 5718 are compared to this baseline to characterize the flare effects in the upper atmosphere. To characterize changes to the atmospheric density and composition during the flare-affected orbit, we examine number densities for each of the six major and minor neutral species provided in the selected NGIMS data version: helium (He), atomic oxygen (O), molecular nitrogen (N₂), carbon monoxide (CO), argon (Ar), and carbon dioxide (CO₂).

At the time of the baseline orbits, the Martian upper atmosphere was not contaminated by other significant sources of density and compositional change such as significant dust storms (not present), CMEs (arrived later), or SEPs (primarily affect altitudes lower than those observed by NGIMS) (C. O. Lee, Jakosky, et al., 2018; Mayyasi et al., 2018; Sánchez-Cano et al., 2019). Other flares of magnitude M and greater from same solar event were also not present at the time of or directly preceding the five baseline orbits (Chamberlin et al., 2018). Over the altitude range of valid number density measurements, each inbound periapsis pass spanned solar zenith angles of ~65–70°, at ~16.7–17.6 local solar time (LST). Consequently, the nonflare orbits experienced relatively constant levels of solar irradiance (Jain et al., 2018). While the latitudes of these measurements were also relatively consistent for each inbound orbit, longitude varied significantly between successive profiles as Mars rotated beneath the near-fixed orbital plane of MAVEN. Prior studies have noted large thermosphere density variation between MAVEN orbits caused by sources such as waves, tides, and longitudinal variations (Bougher, Pawlowski, et al., 2015; Bougher, Roeten, et al., 2017; Elrod et al., 2018; Fang et al., 2019; Zurek et al., 2017). Uncertainty caused by such density variations between the baseline orbits is represented by their standard deviation.

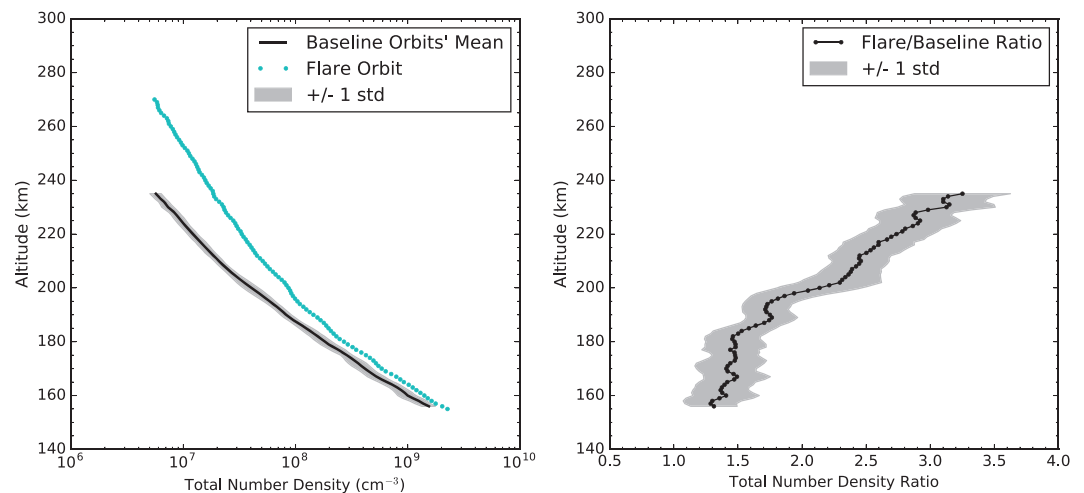


Figure 1. (left) Dependence of total number density on altitude for the flare-affected orbit, 5718 (cyan dots), and for the baseline mean from the surrounding MAVEN orbits, 5715–5720 (black line). Uncertainty is given by the standard deviation of the baseline orbits in gray. (right) Ratio of total number density in the flare-affected orbit at a given altitude to the total number density for the baseline mean at the same altitude.

4. Total Number Density

The left panel of Figure 1 shows the dependence of total number density, composed of the number densities of the six neutral species (He, O, N_2 , CO, Ar, and CO_2), on altitude.

The total densities at each altitude are calculated by interpolating the inbound number densities for MAVEN Orbits 5715–5720 onto a grid of common altitudes separated by 1 km increments, which is close to the NGIMS vertical resolution in the thermosphere (Liu et al., 2018). The range of fixed altitudes was selected to span that of the species and orbit with the most limited data (~ 155 – 235 km). The species densities from the flare-affected orbit (5718) are combined at each fixed altitude to provide the flare-affected total density profile. The mean of the densities from the surrounding orbits (5715, 5716, 5717, 5719, and 5720) are summed over the individual species for each fixed altitude to form the baseline total density profile.

Uncertainty for the baseline total density profile is calculated from the standard deviation of the densities from the set of baseline orbits for each altitude, which is then combined over the individual species using standard methods for the propagation of uncertainty. This baseline density uncertainty represents fluctuations in thermosphere densities stemming from geophysical sources such as thermal tides, gravity waves, and other aspects of weather, in addition to instrumental random errors. Due to the lack of experimental scatter measurements upon which to base uncertainty for individual orbits, we provide no uncertainty for the flare-affected orbit.

The left panel of Figure 1 demonstrates that the impact of the flare on thermospheric densities is clearly significant. For example, during the flare-affected orbit, the total number density at 235 km increases by as much as a factor of 3, and the altitude at which total number density typically equals 10^7 cm^{-3} is increased by 30–40 km. Total number densities are larger than normal at all altitudes during the flare orbit, including down at periaapsis near 155 km.

Increases in total number density are not uniform at all altitudes. The right panel of Figure 1 presents a ratio of the flare and baseline total density profiles, illustrating how the increase in total density is greater at higher altitudes. This ratio shows that the relative increase in total number density is approximately uniform below 190 km and grows larger at a roughly linear rate with increasing altitudes above 190 km.

5. Number Densities of Individual Species

5.1. Effects at Fixed Altitude

Next, we examine how the number densities of individual species changed during the flare. The left panel of Figure 2 shows the number density of each neutral species for the flare-affected and baseline orbits across

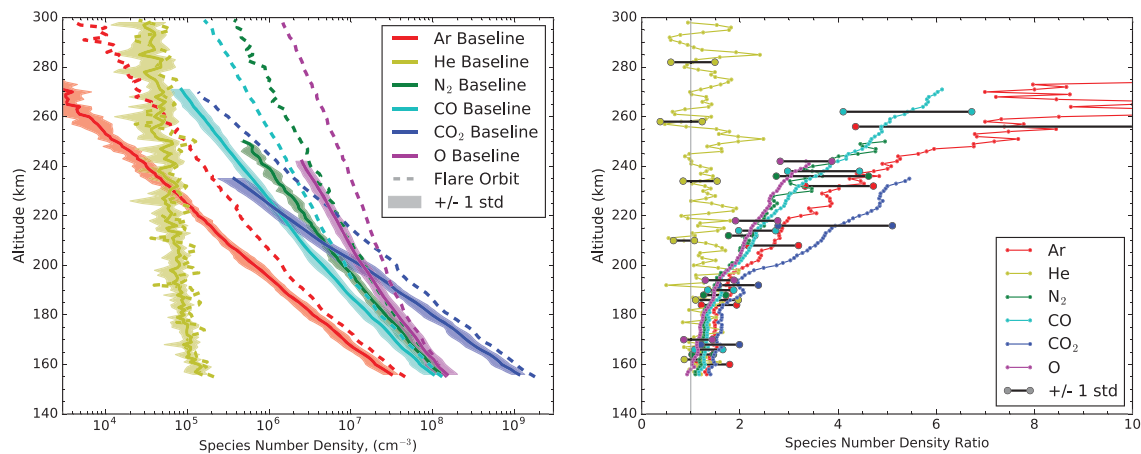


Figure 2. (left) Dependence of the densities of six neutral species (Ar, He, N₂, CO, CO₂, and O) on altitude for the flare-affected orbit (dashed lines) and for the average of the set of baseline orbits (solid lines). (right) Ratio for each individual species of the number density in the flare-affected orbit to the baseline number density for the same species at the same fixed altitudes.

our range of fixed altitudes. We investigate whether all individual species are affected by the flare in the same way as the total number density profile or whether certain species are affected differently. In one possible scenario, if the entire atmosphere was uplifted like a rigid body by the effects of the flare, then we would expect that number densities of all species would increase by the same factor as the total number density. In another possible scenario, if some species were unaffected by the effects of the flare, then we would expect that number densities of those species would not change at all.

The baseline density profiles are in general agreement with prior studies of the composition of the Martian upper atmosphere (Mahaffy, Benna, Elrod, et al., 2015; Mahaffy, Benna, King, et al., 2015). CO₂ is the dominant species at lower altitudes and is surpassed by atomic O above approximately 200 km. The number densities of N₂ are also appreciable but smaller, and Ar and He are trace species.

Throughout the present work, we divide reported CO number densities by a factor of 4. If such a correction factor is not applied, then CO number densities appear to be unusually large. Unadjusted, CO would be the most abundant species in the altitude range of ~ 190 – 215 km for the baseline density profile, which is not consistent with earlier observations or theoretical models (Bougher et al., 1990; Bougher, Pawlowski, et al., 2015; Mahaffy, Benna, Elrod, et al., 2015; Nier & McElroy, 1977). Moreover, CO number densities would not be consistent with the earlier studies of Elrod et al. (2018) with these same orbits. We note that CO densities reported by NGIMS increased by approximately a factor of ~ 7 between the Version 07 Revision 03 products used by Elrod et al. (2018) and the Version 08 Revision 01 products used in this work. The NGIMS team is currently assessing the calibration of CO density values. They advise that CO densities in Version 08 Revision 01 products be divided by a factor between 2 and 5. In the present work, we adopted a factor of 4. This value ensures that CO is never the most abundant species, as suggested by previous work, and is squarely in the center of the recommended range. The sensitivity of our findings to the adopted value of this correction factor is further discussed in section 7.2.

As is observed for our baseline total density profile in the left panel of Figure 1, the number density of each species decreases approximately exponentially with increasing altitude in the left panel of Figure 2. Densities of the lower mass species change more gradually with altitude and as such have greater scale heights. Some mass dependence to this baseline density structure is expected, as the full range of altitudes from our observations are above the homopause (Slipski et al., 2018), where well-mixed species separate by mass as molecular diffusion replaces eddy diffusion as the primary diffusive process regulating the atmosphere (Strobel, 2002).

If these density distributions are controlled solely by diffusive processes, then we would expect the product of molecular mass and scale height to be proportional to temperature and therefore the same for all species. However, even though the qualitative expectation of lower mass species having greater scale heights is

satisfied, the quantitative expectation of species-independent products of molecular mass and scale height is not satisfied. This is consistent with the observation of Elrod et al. (2018) that temperatures derived from density scale heights are different for different species. These findings indicate that chemical processes play a role in influencing the density distribution.

Since O is a highly reactive species for which observed densities require steady production by the photodissociation of molecules containing oxygen, this indication that photochemistry is involved in producing the observed results is not surprising.

During the flare-affected orbit, the same qualitative features are present in the number density profiles of each species. As was observed in the flare-affected total density profile from the left panel of Figure 1, the number densities of O, N₂, CO, Ar, and CO₂ increased relative to their baseline values during the flare orbit, and these increases were most prominent at higher altitudes.

Yet the He number densities in the flare-affected orbit show no apparent change from the He baseline profile. In the baseline orbits, He number density decreases from $1.48 \times 10^5 \text{ cm}^{-3}$ at 156 km to $3.44 \times 10^4 \text{ cm}^{-3}$ at 298 km, implying a scale height of 100 km. For the other species, the high-altitude scale height is increased by a factor of about 1.4 in the flare-affected orbit. If the He scale height was increased by this factor at all altitudes and the number density at 156 km kept constant at $1.48 \times 10^5 \text{ cm}^{-3}$, then we would expect the He number density at 298 km to increase from 3.44×10^4 to $5.22 \times 10^4 \text{ cm}^{-3}$. This expected change is smaller than the scatter in observed values of the He number density. Therefore it is possible that the lack of apparent change in He number densities is actually consistent with the typical increase in scale height by a factor of 1.4 seen in other species.

The right panel of Figure 2 plots a ratio of the flare-to-baseline number densities for each individual species, illustrating how the relative increase in the number densities of each species changes with altitude. As we have noted from the left panel of Figure 2, there is no apparent change in the He number density profile at any altitude. The flare-to-baseline density ratios for each of the five other species resemble the general shape of that seen in the right panel of Figure 1 for the total number density: modest and uniform relative increases below 190 km and larger and growing relative increases above 190 km.

The altitude dependence of the amount by which number densities changed during the flare orbit differs by species, as is demonstrated by the differing slopes of each species, particularly above 190 km. The relative increase for CO₂ is greater than for Ar, which is greater than for CO and N₂ (which are similar), which are greater than for O. Although this trend is not statistically significant, it is noteworthy that the magnitude of the relative increase is greater for species of greater molecular mass. This trend could also in part explain why the number density of low-mass He does not appear affected by the flare.

5.2. Effects at Fixed Total Number Density

The observations presented in section 5.1 were discussed in terms of altitude, which illustrates changes caused both by thermal expansion of the bulk atmosphere and by chemical changes in atmospheric composition. In order to isolate the chemical changes caused by the solar flare, we now discuss the NGIMS observations in terms of fixed pressure levels. This eliminates the effects of thermal expansion, which merely displaces pressure levels in altitude.

We use total number density as a proxy for pressure. We do not use pressures derived from the hydrostatic equilibrium equation, as terms from the momentum equation, which are neglected when assuming a hydrostatic atmosphere, may not be negligible at the high altitudes of our observations, which extend above the exobase (Strobel, 2002). In addition, the NGIMS number density measurements for individual species extend to different vertical upper limits, which would need to be approximated using a single upper boundary condition for the differential equation that would yield the pressure profile. A single upper bound would also be required in order to use total column number densities as a proxy for pressure.

By contrast, total number density can be determined directly from the available density measurements without consideration of boundary conditions. Given that within a planetary atmosphere temperature generally changes linearly with altitude, whereas density changes exponentially, we judge that total number density is sufficiently proportional to pressure ($p \propto nT$) to be used here to isolate the effects of chemical changes.

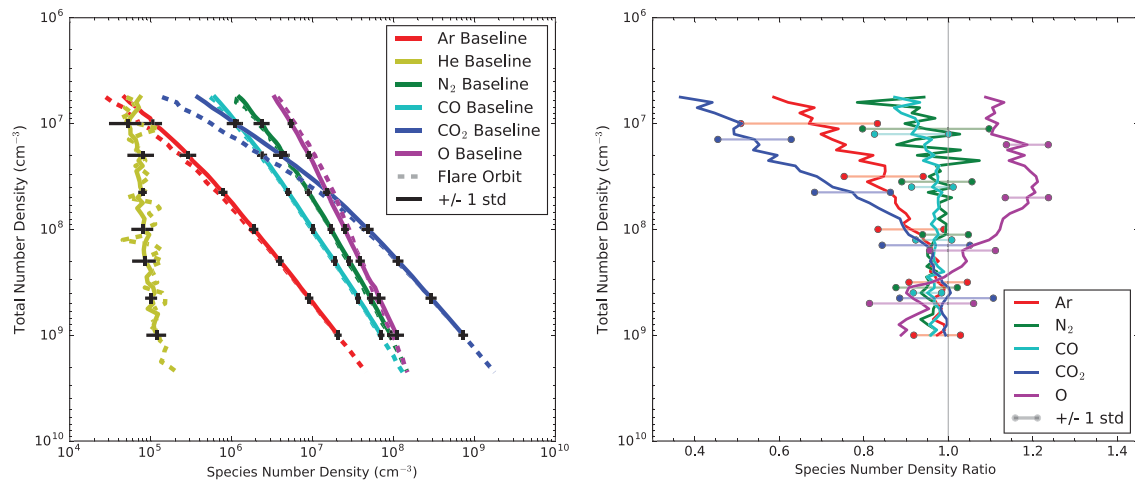


Figure 3. (left) Dependence of the densities of each individual species on total number density for the flare-affected orbit (dashed lines) and for the average of the set of baseline orbits (solid lines). (right) Ratio for each individual species of number density in the flare-affected orbit at a given total number density to the baseline mean number density of that species at the same total number density.

To produce a grid of fixed total densities, total densities were first calculated by summing the six NGIMS species at each altitude from the fixed altitude grid previously generated as described in section 5.1. Then, for each species and orbit, total densities were interpolated onto a log scale increasing by exponent increments of 0.05 ($10^{6.50}$, $10^{6.55}$, ...). Creating a fixed total density grid allows a baseline average of species densities, a flare-to-baseline density ratio, and error bars to be generated across common total density values. In each figure for which we have replaced altitudes with total number densities, we have inverted the vertical axis of fixed total densities in order to mirror the baseline atmosphere structure, with densities decreasing toward higher altitudes.

The left panel of Figure 3 shows the same number density profiles of individual species as the left panel of Figure 2 but now expressed relative to total number density rather than altitude. Changes in the species number densities during the flare-affected orbit appear significantly smaller in the left panel of Figure 3 than in the left panel of Figure 2. This indicates that thermal expansion of the bulk atmosphere plays a significant role in creating the apparent density changes of the left panel of Figure 2 compared to the role of changing chemistry.

At total number densities greater than $\sim 10^8 \text{ cm}^{-3}$ (low altitudes), the number densities of each species remain unaltered, whereas in the left panel of Figure 2, the number densities of Ar, CO, N₂, and CO₂ were still slightly enhanced at low altitudes. This suggests that while thermal expansion is present from flare heating at lower thermospheric altitudes, the chemical processes in this region remain unaffected. At total number densities less than 10^8 cm^{-3} (high altitudes), it appears that of the species examined, only CO₂, O, and Ar densities change relative to their baseline density values. This also contrasts with the left panel of Figure 2, where relative changes in N₂ and CO densities were more significant than those of O.

The right panel of Figure 3, which presents a ratio of the flare-to-baseline species densities in terms of fixed total densities, indicates that the number density of O is enhanced to roughly a factor of 1.2 at high altitudes, and CO₂ and Ar densities are diminished by up to 60% and 40%, respectively.

The relative decrease in Ar at high altitudes is unexpected because the species, as a noble gas, should be relatively inert. In contrast, chemical reactions involving O or CO₂ are common, and thus the changes in their relative densities during the flare-affected orbit are expected when expressed in terms of fixed total densities.

The right panel of Figure 3 suggests that the relative change in the O density during the flare-affected orbit may not continuously increase with altitude. Instead, it may reach a maximum value for total number densities in the range 2×10^7 to $2 \times 10^8 \text{ cm}^{-3}$. However, the statistical significance of this finding is weak.

It is important to note that by construction, it is not possible for all number densities to increase (or decrease) from the baseline to the flare profile at a given total number density level in the left panel of Figure 3. If the

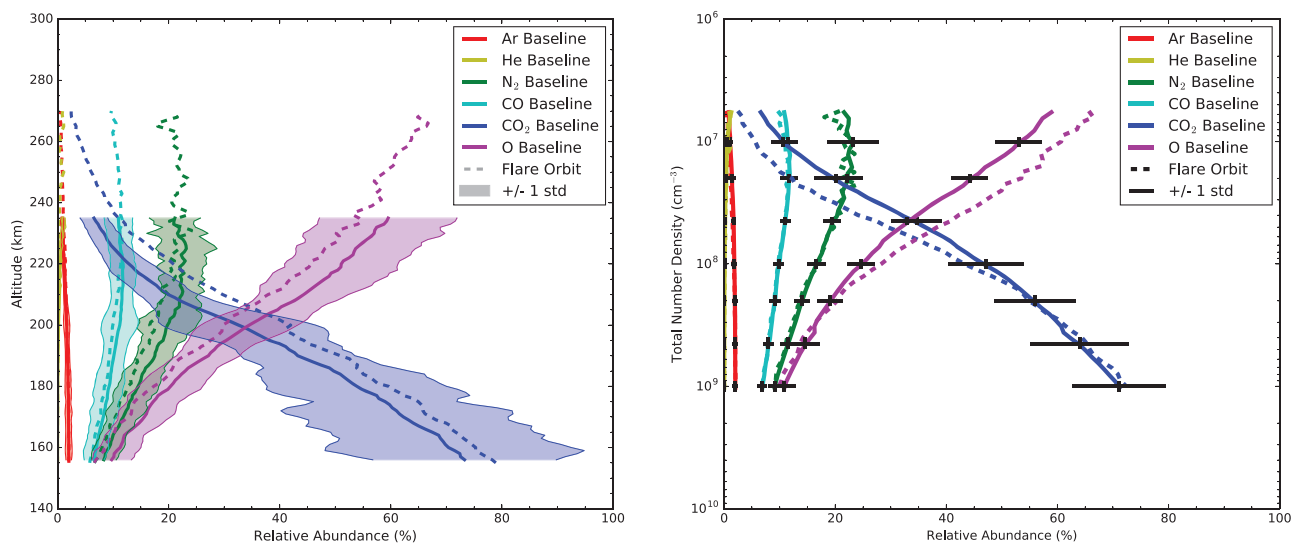


Figure 4. (left) Dependence of the relative abundances (species/total number density) of each individual species on altitude for the flare-affected orbit (dashed lines) and for the average of the set of baseline orbits (solid lines). (right) Dependence of the relative abundances of each individual species on total number density for the flare-affected orbit (dashed lines) and for the average of the set of baseline orbits (solid lines).

number density of one major species increases, then the number density of at least one other major species must decrease to compensate. As such, the observed increase in the O number density is coupled to the observed decreases in the CO₂ and Ar number densities.

6. Composition

6.1. Effects at Fixed Altitude

The previous sections examined how the densities of individual species were affected by the 10 September 2017 solar flare. Here we examine how the atmospheric composition was affected by the solar flare. To do so, we investigate changes in the relative abundances (%) of each individual species at fixed altitude. The relative abundance of each species is calculated by dividing the species density by the total density calculated at the same altitude.

The left panel of Figure 4 shows the relative abundances of each species for the flare-affected orbit and for the baseline set of orbits. Viewed here in terms of altitude, the compositional effects of the flare appear minor. While the relative abundances of O, N₂, and CO appear to decrease slightly for the flare-affected orbit, they remain within one standard deviation of their baseline relative abundances at all altitudes. Changes in the relative abundances of Ar and He are difficult to discern in the left panel of Figure 4 due to their small proportions in the total neutral atmospheric composition, but each changes by less than ~1%.

The relative abundance of CO₂ is notably larger for the flare-affected orbit than its baseline value and exceeds the average by more than one standard deviation at altitudes above 200 km. This is the expected behavior of CO₂ under the influence of thermal expansion, given its high relative abundance at low altitudes in the thermosphere.

6.2. Effects at Fixed Total Number Density

As in section 5.2, we also examine the compositional effects of the solar flare in terms of fixed total number density. The right panel of Figure 4 shows the relative abundances of each species for the flare-affected orbit and baseline orbits average, as in the left panel of Figure 4, but in terms of fixed total number density rather than fixed altitude.

At total number densities greater than 10^8 cm^{-3} (low altitudes), the atmospheric composition is not altered significantly by the flare. At total number densities less than 10^8 cm^{-3} (high altitudes), the relative

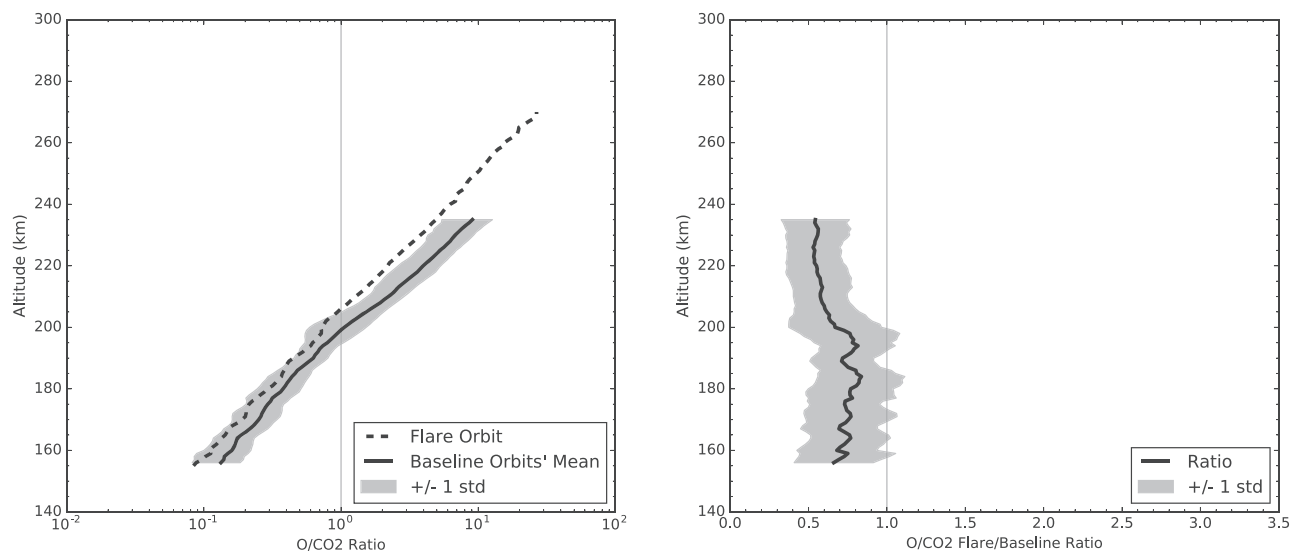


Figure 5. (left) Dependence of the O/CO₂ ratio on altitude for the flare-affected orbit (dashed line) and for the average of the set of baseline orbits (solid line). (right) Ratio of the O/CO₂ ratio on the flare-affected orbit at a given altitude to the average O/CO₂ ratio in the set of baseline orbits at the same altitude (solid line).

abundance of O is enhanced by the flare and the relative abundances of CO₂ and Ar are diminished, while the relative abundances of N₂, CO, and He exhibit no statistically significant change.

Rather than using axis values from the fixed total density scale, total number densities in this figure are the sum over the individual, orbit-averaged species densities at each fixed total density. The difference between total number densities calculated from these two methods is relatively minor, but only the latter produces relative abundances which add up to 100%.

The increase in the proportion of O and decrease in the proportion of CO₂ in the upper thermosphere are seen in the right panel (fixed total densities) but not in the left panel (fixed altitudes) of Figure 4. This chemical enhancement of O densities and chemical decrease in CO₂ are also seen in Figure 3 (fixed total densities) and are similarly overshadowed by the larger density changes from thermal expansion in Figure 2 (fixed altitudes). However, whereas comparison between Figures 2 and 3 shows that flare-produced changes are much smaller when viewed against fixed total densities than against fixed altitudes, changes in the altitude and total density-viewed relative abundances of species (Figure 4, left and right panels) are of comparable size to one other. This demonstrates that while the chemical effects produced by a solar flare have a relatively minor effect on the densities of individual species in the thermosphere, their influence on the atmospheric composition is more sizable.

7. O/CO₂ Ratio

The O/CO₂ density ratio provides a useful indication of upper atmospheric change due to O and CO₂ being the most abundant species in the upper and lower altitudes of the thermosphere, respectively, as well as significant components of the region's foremost chemical reactions (Bougher, Pawlowski, et al., 2015; Krasnopolsky, 2002). The O/CO₂ ratio has been used to track the behavior of global atmospheric circulation in models and is an analog to the O/N₂ ratio used at Earth to track the atmospheric response to geomagnetic storms (Siskind & Bougher, 2016). From the previous sections, O and CO₂ are shown to be the two neutral species most affected by the solar flare. As such, the behavior of the O/CO₂ ratio serves as a useful measure of the effects from the solar flare.

7.1. Effects at Fixed Altitude

The left panel of Figure 5 shows the O/CO₂ ratio for the flare-affected orbit and the baseline average.

This panel demonstrates that the flare-affected O/CO₂ ratio is smaller than the baseline O/CO₂ value at all altitudes but is only more than one standard deviation away from the baseline average at altitudes above

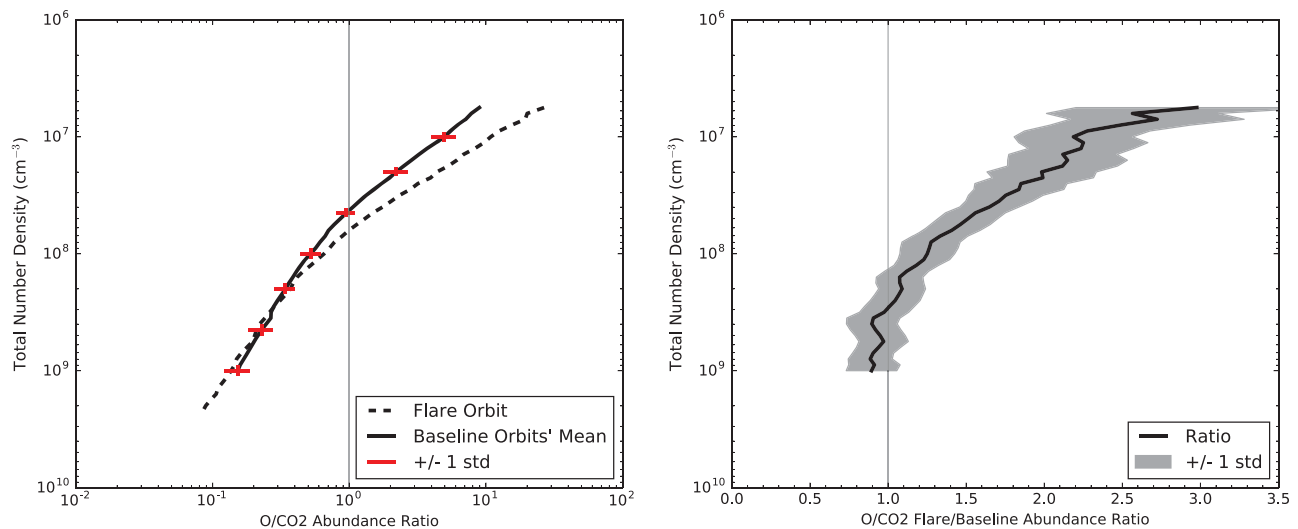


Figure 6. (left) Dependence of the O/CO₂ ratio on total number density for the flare-affected orbit (dashed line) and for the average of the set of baseline orbits (solid line). (right) Ratio of the O/CO₂ ratio on the flare-affected orbit at a given total number density to the average O/CO₂ ratio in the set of baseline orbits at the same total number density (solid line).

~205 km. The altitude at which the O/CO₂ ratio is unity is elevated from a baseline value of 200 ± 5 to 205 ± 5 km. To provide uncertainties for the altitudes at a given density ratio, despite densities not being fixed across altitudes, the density uncertainty values above and below the density ratio are averaged into an altitude uncertainty value.

Thermal expansion during the flare-affected orbit would be expected to increase the altitude at which the O/CO₂ ratio equals unity, as is observed. However, the altitude at which the O/CO₂ ratio is unity has been observed to vary substantially over a short, multihour timescale in the absence of solar or dust storm conditions. Influence from the lower atmosphere interaction between gravity waves and the global winds, and small-scale atmospheric mixing are potential sources of this variation (Bougher, Jakosky, et al., 2015).

It is relevant to note that observations drawn directly from the left panel of Figure 5, if taken out of context from prior figures, could result from a number of atmospheric behaviors which produce the same result, such as an increase in the abundance of O, a decrease in the abundance of CO₂, or a combination of the two. From Figure 2, it is apparent that the decrease in flare-orbit O/CO₂ ratio values in the left panel of Figure 5 is a result of the enhancement of CO₂ densities exceeding the enhancement of O densities.

The right panel of Figure 5 compares the O/CO₂ ratio on the flare-affected orbit directly to the baseline O/CO₂ ratio. The slope of this flare-to-baseline O/CO₂ ratio plot is close to vertical at all altitudes but is centered at a smaller value (~0.5) for altitudes above approximately 200 km and a larger value (~0.7–0.8) for lower altitudes. This indicates that consistently across all altitudes above 200 km, the O/CO₂ ratio was reduced to roughly half its baseline value during the flare-affected orbit. It also indicates that consistently across all altitudes below 200 km the O/CO₂ ratio was less significantly affected by the flare and remained roughly 0.7–0.8 times the baseline O/CO₂ ratio. This non-unity ratio value at the lowest measured altitudes shows agreement with MAVEN/IUVS findings of atmospheric heating below 170 km during the flare-affected orbit (Jain et al., 2018).

7.2. Effects at Fixed Total Number Density

The left panel of Figure 6 shows the O/CO₂ ratio for the flare-affected orbit and for the baseline average, as in the left panel of Figure 5, but in terms of fixed total number density rather than fixed altitude.

The flare-affected O/CO₂ ratio is greater than the baseline average by more than one standard deviation at total number densities less than $\sim 10^8 \text{ cm}^{-3}$ (high altitudes) and is within one standard deviation of the baseline average for larger total number densities (low altitudes). In contrast with the fixed altitude representation in the left panel of Figure 5, where the O/CO₂ ratio is reduced by the flare, the fixed total

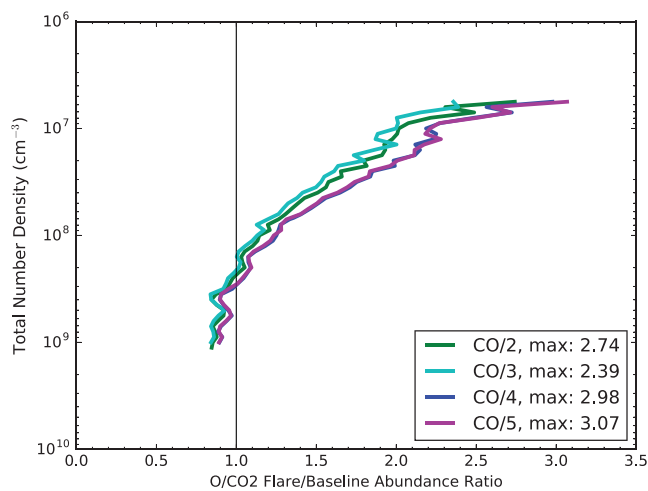


Figure 7. Dependence of flare orbit O/CO₂ to baseline O/CO₂ ratio on different CO density correction factors. The correction factor of 4 is used throughout this work.

number density representation in the left panel of Figure 6 shows an increase in the O/CO₂ ratio during the flare orbit.

At the lowest densities sampled by these measurements ($\sim 5.5 \times 10^6 \text{ cm}^{-3}$), the O/CO₂ ratio is 26.6 on the flare-affected orbit, many standard deviations greater than its value of 9 ± 2 for the baseline set of orbits. In other words, these uppermost NGIMS thermospheric measurements indicate that where there is typically as much as 9 times more oxygen than carbon dioxide, during the flare orbit, there is about 26.6 times more oxygen than carbon dioxide.

The right panel of Figure 6 compares the flare-affected O/CO₂ ratio directly to the baseline O/CO₂ ratio by taking the ratio of the two, as was done in the right panel of Figure 5 but now in terms of fixed total number densities rather than fixed altitudes.

At total number densities greater than 10^8 cm^{-3} (low altitudes), the O/CO₂ ratio on the flare-affected orbit is within one standard deviation of its baseline value. This demonstrates that changes to the O/CO₂ ratio due to the flare, in the absence of thermal expansion, are minimal lower in the atmosphere but grow more significant up where the atmosphere

is thinner. At the smaller total number densities, the ratio of the O/CO₂ ratio for the flare-affected orbit to the baseline average increases steadily. This ratio depends approximately linearly on the total number density at total number densities from approximately 10^8 cm^{-3} to our smallest total number density measurements at $\sim 5.5 \times 10^6 \text{ cm}^{-3}$.

At the lowest total number density measurements (highest altitudes), the O/CO₂ ratio increases during the flare-affected orbit by up to a factor of $\sim 2.98 \pm 0.77$.

The results shown in the right panel of Figure 6 are sensitive to the correction factor applied to the reported CO densities (section 5.1). The NGIMS team advised dividing reported CO densities by a factor between 2 and 5. We adopted a factor of 4. Figure 7 illustrates how the right panel of Figure 6 changes if this correction factor is adjusted.

If the correction factor is increased, then the O/CO₂ flare/baseline ratio at a fixed total number density also increases. If a value of 2 is adopted for the correction factor, then the increase in the O/CO₂ ratio at the lowest total number density sampled is 2.7, whereas if a value of 5 is adopted, then this result changes to 3.1. It is apparent from Figure 7 that the calibration of CO densities does not materially affect the findings of the present work.

The O/CO₂ ratio during the 10 September 2017 flare event has been previously examined by Thiemann et al. (2018) at fixed pressure levels. From Figure 3c of that work, the O/CO₂ ratio during the flare-affected orbit grows increasingly greater with lower pressures to a maximum value of ~ 26.9 at a pressure of $1.3 \times 10^{-8} \text{ Pa}$. This is roughly a factor of 4.5 greater than the O/CO₂ ratio of ~ 6 found at the same pressure level during the baseline, surrounding orbits. The O/CO₂ ratio calculated in our work examines changes that are more layer specific or local than pressure-based ratios because the calculation of each fixed total number density is independent of all lower total number densities (the atmosphere above them). To provide consistent comparison with the change in the O/CO₂ ratio drawn from Thiemann et al. (2018), we examine the O/CO₂ ratio for the fixed total density level at which our baseline O/CO₂ ratio is also 6. At this total density level, the flare orbit O/CO₂ ratio is 14.6, or a factor of 2.4 above the baseline ratio. That this O/CO₂ ratio enhancement is smaller than the ratio calculated from Figure 3c of Thiemann et al. (2018) is expected, as O and CO₂ chemistry that occur higher in the Martian atmosphere likely contribute to the greater factor found with fixed pressures.

8. Flare Effects in Context

Two significant influences on the Martian thermosphere are variations in the received amounts of solar irradiance at EUV wavelengths and variations in the dust loading of the atmosphere (Bougher et al., 1997).

Table 1
Perturbed/Baseline Number Density Ratios

Event	170 km		220 km		Source
	O	CO ₂	O	CO ₂	
Flare	1.15	1.52	2.44	4.43	This study
Solar cycle	2.4	2.8	3.8	16.6	Krasnopolsky (2002)
	1.6	2.3	2.7	13.2	Bougher, Pawlowski, et al. (2015)
Dust storms (regional)	~1.2	1.3	>2.0	>3.4	Liu et al. (2018) (nightside)
	1.1	1.3	1.1	1.6	Liu et al. (2018) (dayside)
	1.3	1.8	1.8	2.8	Y. Lee et al. (2020)
Dust storms (global)	0.6	5.0	0.7	5.2	Y. Lee et al. (2020)
	0.7	1.5	n/a	n/a	Elrod et al. (2020) ^a

^aDensities calculated for SZA ~ 67°.

To provide greater context for the effects of solar flares in the Martian thermosphere, we compare the density changes observed for major thermosphere species O and CO₂ during the 10 September 2017 flare to the changes caused by these two significant influences. The comparisons described in the following subsections are also listed in Table 1.

8.1. Flare Effects Compared With Solar Cycle EUV Variation

We use O and CO₂ number densities extracted from graphical representations of outputs from the models of Krasnopolsky (2002) and Bougher, Pawlowski, et al. (2015) to compare maximum density changes due to the solar cycle with MAVEN flare event data. $F_{10.7}/d^2$, used as a rough proxy for solar EUV irradiance received at Mars, is set to 25 (solar minimum) and 88 (solar maximum) by Krasnopolsky (2002). We estimate from $F_{10.7}$ and solar longitude values that Bougher, Pawlowski, et al. (2015) conditions have slightly larger $F_{10.7}/d^2$ values of ~33 (solar minimum) and ~95 (solar maximum). Densities are found for a dayside mean at SZA = 60° by Krasnopolsky (2002) and for LST = 15 at SZA = 45° by Bougher, Pawlowski, et al. (2015). In greater contrast, Krasnopolsky (2002) presents a 1-D model that utilizes eddy diffusion to produce the global effects of winds on the atmosphere's density distributions, while Bougher, Pawlowski, et al. (2015) present a 3-D global model within which both horizontal and vertical winds, with more limited eddy diffusion, shape the density distributions in the atmosphere. These structural differences between the two models may result in a broader range of thermosphere behavior over the solar cycle, providing a more robust comparison to the flare-affected atmosphere.

For both models, we find that number densities of both O and CO₂ changed more greatly from solar minimum to maximum of the solar cycle than from baseline to flare-affected conditions during the 10 September 2017 flare, at all altitudes examined. Over the altitude range of 170–220 km, the Krasnopolsky (2002) model indicated factors of ~2.4–3.8 increase in O densities from minimum to maximum of the solar cycle, while the Bougher, Pawlowski, et al. (2015) model, M-GITM, indicated factors of ~1.6–2.7 increase. During the 10 September 2017 flare O densities in contrast increased by factors of ~1.15–2.45, amounting to roughly 50–90% of the density enhancements from the solar cycle EUV variations, with the most prominent fraction at higher thermospheric altitudes. Over the same altitude range, CO₂ densities increased by more significant factors of ~2.8–16.6 and ~2.3–13.2, according to each model, respectively. CO₂ densities from the flare in contrast increased by more modest factors of 1.50–4.45, or roughly ~25–65% of the density enhancements due to the solar cycle. The flare-produced changes in CO₂ densities comprise greater proportions of the solar cycle-produced CO₂ changes at lower altitudes.

8.2. Flare Effects Compared With Dust Storm Effects

Another significant source of upper atmospheric change at Mars besides EUV variation is dust storms (Withers & Pratt, 2013). These effects differ for global and regional dust storms. To compare dust storm

density changes with those produced by the 10 September 2017 flare, we compare flare event observations with observed and modeled densities of O and CO₂ derived from figures in Liu et al. (2018), Y. Lee et al. (2020), and Elrod et al. (2020).

Observations of thermosphere density (measured as % variation, [dust-clear]/clear) for three regional dust storms in late 2015 and early 2017 differed greatly due to varied local times (day and night) and amounts of dust loading and activity. However, Liu et al. (2018) show that in the dust-affected atmosphere, O and CO₂ densities were greater at all thermospheric altitudes, increasing by less than 30% at ~170 km and by up to 200% at ~220 km. The densities also increased more greatly for CO₂ than for O at all altitudes examined. Over the same altitude range of 170–220 km, modeling by Y. Lee et al. (2020) also indicates enhanced densities during regional dust storms, by roughly 25–80% (O) and 80–185% (CO₂) above baseline levels. In contrast, the aforementioned density enhancements from baseline to solar flare-affected conditions were smaller than regional dust storm effects below ~190 km but exceeded them at higher altitudes.

Modeled global dust storm conditions, based from the 1971–1972 global dust storm on Mars, indicate in contrast with the flare, solar cycle, and regional dust storm effects in the thermosphere that the abundance of O decreases compared to in the undisturbed, baseline atmosphere, at altitudes above 150 km (Y. Lee et al., 2020). In the 170–220 km altitude range, the O densities decrease by roughly ~35–40% and most greatly at middle thermospheric altitudes (~190 km). By comparison, O densities in the flare-affected atmosphere increase by a broader range of 15–145% and are greatest at higher thermospheric altitudes. As such, O densities are more greatly affected by the flare than by the global dust storm at altitudes above roughly ~190 km altitude. CO₂ densities are increased by a relatively constant ~4 factors at all thermospheric altitudes during the global dust storm. For CO₂, flare-produced density changes are smaller than those produced by the global dust storm at all altitudes examined. Flare-produced changes in CO₂ densities make up only ~30–85% of the global dust storm's changes, with the larger proportion at higher altitudes.

Thermospheric density changes produced by the 2018 global dust storm at Mars are reported by Elrod et al. (2020) and indicate that O and CO₂ densities decreased and increased by ~25% and ~55%, respectively, during the peak of the global dust event conditions at an altitude of 170 km with SZA = ~67°, the same SZA of the flare event observations. These changes likewise suggest that effects of the flare were smaller than those of a global dust event below high thermospheric altitudes.

8.3. Flare Context Synthesis

Overall, density changes from the large solar flare on 10 September 2017 in the Mars thermosphere appear to be smaller than the maximum variation across the solar cycle at all altitudes. The flare effects are smaller than regional dust storm effects below ~190 km. However, the solar flare produced greater change than the effects produced by regional dust storms for both O and CO₂ at altitudes above ~190 km, and O density changes during the 1971–1972 global dust storm at altitudes above ~190 km.

These comparisons best serve as a loose estimate of the relative extent of flare behavior in the upper Martian thermosphere compared with other significant sources of change. The X8.2 flare upon which we base comparisons is larger and thus more influential on the upper atmosphere than the majority of flares that impact Mars, even with the delay between its arrival and observations. While flares have historically had greater magnitudes than those in the present day, typical EUV irradiance in the past was also as much as 100–1,000× larger than present baseline amounts (Ribas et al., 2005), which would likewise affect the magnitudes of solar cycle and dust storm variations.

In addition, variations between the magnitudes of different flares and dust storms and between different solar cycles are significant. Even under relatively constant solar conditions, dayside atmospheric variations from sources such as waves or tides can vary thermosphere densities by factors as great as 1.35–2.75 over the timescale of successive MAVEN orbits (Elrod et al., 2018), as is similarly noted in section 7 of the variable altitude at which O and CO₂ have the same density. As such, the relative significance of these sources on the thermosphere is not possible to closely constrain with limited comparisons. Overall, we surmise that the atmospheric influence of the 10 September 2017 flare is roughly scalable with other recent events at Mars, and as such, it is important to consider flares as a significant, if infrequent and short-lived, source of thermosphere change.

9. Discussion

The apparent responses of species densities and atmospheric composition to the 10 September 2017 solar flare differ greatly depending on the frame of reference in which they are viewed. At fixed altitudes, the densities of O and CO₂ were both increased by the solar flare, while at fixed total number density, the density of O was increased and the density of CO₂ was decreased. The O/CO₂ ratio was decreased by the flare at fixed altitude but was increased by the flare at fixed total number density.

These contrasting results indicate that two effects occur simultaneously in the thermosphere during a solar flare. First, heating occurs, which expands the atmosphere and tends to increase the densities of all species at fixed altitude. Second, photochemistry occurs, which alters the chemical composition of the atmosphere at fixed pressure, or total number density, levels.

The left panel of Figure 1 shows that the relative increase in total number density on the flare-affected orbit, when viewed at fixed altitudes, is larger at higher altitudes.

The steeper slope of the density data from the flare-affected orbit implies that the atmospheric temperature increased at all altitudes sampled (~155–235 km), rather than merely a restricted region within the sampled altitudes. These temperature changes due to solar heating are discussed further in Elrod et al. (2018).

Heating of the atmosphere by the solar flare also produced significant changes in the thermospheric density structure. For example, the altitude at which total number density equals 10⁷ cm⁻³ increased by 30–40 km on the flare-affected orbit. Equivalently, total number density at 235 km increased by a factor ~3 on the flare-affected orbit. The neutral species density changes identified in the right panel of Figure 2 are in agreement with the density magnification factors identified by Elrod et al. (2018) for NGIMS neutral species at an altitude of 225 km for this flare. The higher altitude Ar density enhancements that we observe are likewise several factors greater than the 66% increase in Ar density noted by Thiemann et al. (2015) at 250 km altitude for a smaller magnitude (M-class) solar flare on 24 March 2015.

As viewed against fixed total number density, the magnitudes of the observed changes in thermospheric chemical composition are greater as total number density decreases, corresponding to higher altitudes in the atmosphere. The right panel of Figure 3 demonstrates this relationship with the greater deviation of the flare-to-baseline density ratios from unity for Ar, CO₂, and O at smaller total number densities. Yet not all species are affected in this manner, as this ratio remains constant at unity for CO and N₂.

The presence of a change in the number density of Ar when viewed against fixed total number density is unexpected considering the chemical inertness of the species. This suggests that the effects of a mechanism besides photochemistry caused changes to the densities of the species, such as changing atmospheric pressure gradients due to atmospheric heating (Benna et al., 2019; Roeten et al., 2019), which the flare could provide. Further investigation of the source of these changes is beyond the scope of this work.

Since both O and CO₂ are chemically reactive species, changes to their densities in the flare-affected thermosphere as viewed at fixed total number density are likely of primarily photochemical origin. Neutral atomic oxygen in the thermosphere of Mars is short-lived due to its high chemical reactivity and is continually replenished by processes including the photodissociation of neutral CO₂ molecules. As such, increased abundances of O and decreased abundances of CO₂ are expected results of the substantially increased EUV solar irradiance reaching the Martian thermosphere during a solar flare. When the effects of thermal expansion are excluded by viewing the densities of O and CO₂ at fixed total number density levels, such changes are observed at total number densities of less than 10⁸ cm⁻³. For O, these changes are most pronounced at mid-valued total number densities, between ~2 × 10⁷ and 1 × 10⁸ cm⁻³, rather than increasing continually to the smallest total number densities as do the CO₂ densities. However, the observational uncertainties permit the possibility that changes in O density during the flare depend monotonically on total number density.

It is apparent that the change in the O/CO₂ ratio does depend strongly on total number density, with the greatest changes occurring at low total number density (high altitude).

Reproduction of this observed behavior by a physics-based model would provide useful insight into the physical and chemical mechanisms by which a solar flare affects the composition of the atmosphere of Mars.

For instance, vertical transport processes, which are not considered in this work, may also play an important role in altering the thermosphere densities and composition following a flare. Likewise, global circulation models indicate a strong influence of global winds on the Martian thermosphere due to the advection of greater proportions of lighter mass species, such as O, to the nightside of Mars (Bougher, Brain, et al., 2017). The influence of global winds on O densities alters the O/CO₂ ratio—affecting both the density and composition of the Martian thermosphere. Global horizontal winds are influenced by amounts of solar irradiance received (e.g., with the greater EUV heating of solar maximum yielding stronger winds) and resulting chemistry (with a greater amount of a species distributed to the nightside if more is produced due to enhanced dayside photochemistry) (Bougher, Pawlowski, et al., 2015). It could be possible that the density and composition changes observed in this work are also affected by global winds responding to the changes in solar irradiance, atmospheric heating, and chemistry due to the flare. The behavior of Ar and O/CO₂ at low total number densities may likewise be further explained with the consideration of additional thermosphere processes besides the heating and photochemistry examined in this work.

10. Conclusions

During a solar flare, the solar irradiance at SXR, EUV, and FUV wavelengths increases significantly over a period of several minutes and then returns to normal over a period of up to several hours (Mendillo et al., 2006; Moore et al., 2014). Due to the increased photon fluxes at these high-energy wavelengths, solar flares heat and thermally expand the thermosphere of Mars. During the X8.2 flare of 10 September 2017, Elrod et al. (2018) found that neutral species densities are enhanced by factors ranging from ~ 2.62 (N₂) to 4.95 (CO₂) at an upper thermospheric altitude of 225 km. Our altitude-referenced analysis is in agreement with these values. In addition, solar flares drive chemical changes in thermospheric composition. These compositional changes could arise from direct photochemical effects (again caused by increased photon fluxes at these wavelengths) or from changes in the vertical fluxes of the neutral species lifted by the flare-produced thermal expansion. In this work, we find that these chemical changes can be large.

At the lowest total number densities sampled by MAVEN NGIMS measurements at the time of the 10 September 2017 solar flare ($\sim 5.5 \times 10^6 \text{ cm}^{-3}$), we find that the O/CO₂ ratio is 26.6 on the flare-affected orbit—many standard deviations greater than the baseline value of 9 ± 2 averaged from the flare's surrounding orbits.

Comprehensive understanding of how Mars is affected by solar flares can be advanced in three ways: first, through the comparison of a flare's effects on the neutral thermosphere with those on the charged ionosphere. Since the key neutral species O and CO₂ are important elements of photochemical reactions that involve ion species, ionospheric studies may further shed light on their behavior and that of the upper atmosphere.

Second, through the examination of other flares. Neutral upper atmospheric effects of a flare likely depend on the flare's magnitude and the observing time relative to the time of the flare's peak irradiance, as do their ionospheric counterparts (Mahajan et al., 2009; Mendillo et al., 2006; Thiemann et al., 2015). The time-integrated flux from a flare which is received by the time of observations could also influence effects observed in the neutral upper atmosphere (Fang et al., 2019; Pawlowski & Ridley, 2008). Given MAVEN's 4.5 hr orbit, it is unlikely that significant thermospheric or ionospheric responses to a solar flare will be seen for the same flare on successive orbits. Therefore, analyses of the effects of several distinct flares will be important for characterizing how the thermospheric response depends on a flare's irradiance and other time-dependent features such as the cooling rates of species.

Third, through the use of physics-based numerical modeling. This would help assess the relative significance of heating, photochemical effects, and transport on the behavior of the thermosphere as solar irradiance varies with time during a flare. Initial simulations using a thermosphere-ionosphere general circulation model have been reported by Fang et al. (2019). For both preflare and flare-affected orbits, these simulations tended to underpredict O densities below 200 km altitude but overpredict CO₂ densities above 200 km altitude. The observed relative increases in the densities of all species during the flare were reproduced well by these simulations at altitudes below 200 km. However, the relative increases in density for all species were underpredicted at higher altitudes by the simulation. This was “partly because the model is subject to more

limitations in physics as neutral species gradually change from a fluid-like behavior in the thermosphere toward a ballistic motion across the exobase" (Fang et al., 2019). Despite this, Fang et al. (2019) found that the flare-affected O/CO₂ ratio was reduced by up to 40% relative to the baseline O/CO₂ ratio, which is broadly consistent with the results shown in the right panel of Figure 5.

The findings reported in this work have significance for studies of the climate history of Mars and the evolution of the planet's atmosphere. For instance, CMEs of Carrington event magnitude likely occurred as frequently as once per day in the early solar system, with as many as six CMEs of smaller size impacting Earth per day (Kay et al., 2016, 2019). Associated solar flares would have been equally as frequent. As such, the early atmospheres of the inner solar system planets, such as Mars, were likely exposed to solar flares on a near-continuous basis. This would have affected escape processes and rates at Mars greatly.

Data Availability Statement

The MAVEN data used in this article are publicly available at the NASA Planetary Data System (https://atmos.nmsu.edu/data_and_services/atmospheres_data/MAVEN/ngims.html).

Acknowledgments

This work was supported, in part, by the National Aeronautics and Space Administration (NASA) award NNX16AJ54G (via subcontract from the University of Michigan to Boston University) and by the MAVEN project, which is supported by NASA's Mars Exploration Program. We thank Stephen Bougher and an anonymous reviewer for their helpful comments.

References

- Aa, E., Zou, S., Ridley, A., Zhang, S., Coster, A. J., Erickson, P. J., & Ren, J. (2019). Merging of storm time midlatitude traveling ionospheric disturbances and equatorial plasma bubbles. *Space Weather*, 17, 285–298. <https://doi.org/10.1029/2018SW002101>
- Badruddin, B., Aslam, O. P. M., Derouich, M., Asiri, H., & Kudela, K. (2019). Forbush decreases and geomagnetic storms during a highly disturbed solar and interplanetary period, 4–10 September 2017. *Space Weather*, 17, 487–496. <https://doi.org/10.1029/2018SW001941>
- Benna, M., Bougher, S. W., Lee, Y., Roeten, K. J., Yigit, E., Mahaffy, P. R., & Jakosky, B. M. (2019). Global circulation of Mars' upper atmosphere. *Science*, 366(6471), 1363–1366. <https://doi.org/10.1126/science.aax1553>
- Benna, M., & Elrod, M. K. (2016). NGIMS PDS software interface specification. https://pds-atmospheres.nmsu.edu/data_and_services/atmospheres_data/MAVEN/ngims.html
- Berdermann, J., Kriegel, M., Bany, D., Heymann, F., Hoque, M. M., Wilken, V., & Jakowski, N. (2018). Ionospheric response to the X9.3 flare on 6 September 2017 and its implication for navigation services over Europe. *Space Weather*, 16, 1604–1615. <https://doi.org/10.1029/2018SW001933>
- Berger, T., Matthi, D., Burmeister, S., Rios, R., Lee, K., Semones, E., & Zeitlin, C. (2018). The solar particle event on 10 September 2017 as observed onboard the International Space Station (ISS). *Space Weather*, 16, 1173–1189. <https://doi.org/10.1029/2018SW001920>
- Bland, E. C., Heino, E., Kosch, M. J., & Partamies, N. (2018). SuperDARN radar-derived HF radio attenuation during the September 2017 solar proton events. *Space Weather*, 16, 1455–1469. <https://doi.org/10.1029/2018SW001916>
- Bougher, S. W., Brain, D. A., Fox, J. L., Francisco, G. G., Simon-Wedlund, C., & Withers, P. G. (2017). Upper neutral atmosphere and ionosphere. In R. M. Haberle, R. T. Clancy, F. Forget, M. D. Smith, R. W. Zurek (Eds.), *The atmosphere and climate of Mars* (pp. 433–463). Cambridge: Cambridge University Press. <https://doi.org/10.1017/9781107016187>
- Bougher, S., Jakosky, B., Halekas, J., Grebowsky, J., Luhmann, J., Mahaffy, P., & Yelle, R. (2015). Early MAVEN deep dip campaign reveals thermosphere and ionosphere variability. *Science*, 350(6261), 0459. <https://doi.org/10.1126/science.aad0459>
- Bougher, S. W., Murphy, J., & Haberle, R. M. (1997). Dust storm impacts on the Mars upper atmosphere. *Advances in Space Research*, 19(8), 1255–1260. [https://doi.org/10.1016/S0273-1177\(97\)00278-0](https://doi.org/10.1016/S0273-1177(97)00278-0)
- Bougher, S. W., Pawlowski, D., Bell, J. M., Nelli, S., McDunn, T., Murphy, J. R., & Ridley, A. (2015). Mars Global Ionosphere-Thermosphere Model: Solar cycle, seasonal, and diurnal variations of the Mars upper atmosphere. *Journal of Geophysical Research: Planets*, 120, 311–342. <https://doi.org/10.1002/2014JE004715>
- Bougher, S. W., Roble, R. G., Ridley, E. C., & Dickinson, R. E. (1990). The Mars thermosphere: 2. General circulation with coupled dynamics and composition. *Journal of Geophysical Research*, 95, 14,811–14,827. <https://doi.org/10.1029/JB095iB09p14811>
- Bougher, S. W., Roeten, K. J., Olsen, K., Mahaffy, P. R., Benna, M., Elrod, M., & Jakosky, B. M. (2017). The structure and variability of Mars dayside thermosphere from MAVEN NGIMS and IUVS measurements: Seasonal and solar activity trends in scale heights and temperatures. *Journal of Geophysical Research: Space Physics*, 122, 1296–1313. <https://doi.org/10.1002/2016JA023454>
- Bruno, A., Christian, E. R., de Nolfo, G. A., Richardson, I. G., & Ryan, J. M. (2019). Spectral analysis of the September 2017 solar energetic particle events. *Space Weather*, 17, 419–437. <https://doi.org/10.1029/2018SW002085>
- Chakraborty, S., Baker, J. B. H., Ruohoniemi, J. M., Kunduri, B., Nishitani, N., & Shepherd, S. G. (2019). A study of SuperDARN response to co-occurring space weather phenomena. *Space Weather*, 17, 1351–1363. <https://doi.org/10.1029/2019SW002179>
- Chamberlain, T., & Hunten, D. M. (1989). *Theory of planetary atmospheres: An introduction to their physics and chemistry*. New York, NY: Academic Press.
- Chamberlain, P. C., Woods, T. N., Didkovsky, L., Eparvier, F. G., Jones, A. R., Machol, J. L., & Woodraska, D. L. (2018). Solar ultraviolet irradiance observations of the solar flares during the intense September 2017 storm period. *Space Weather*, 16, 1470–1487. <https://doi.org/10.1029/2018SW001866>
- Chertok, I. M., Belov, A. V., & Abunin, A. A. (2018). Solar eruptions, Forbush decreases, and geomagnetic disturbances from outstanding active region 12673. *Space Weather*, 16, 1549–1560. <https://doi.org/10.1029/2018SW001899>
- Clilverd, M. A., Rodger, C. J., Brundell, J. B., Dalzell, M., Martin, I., Mac Manus, D. H., & Obana, Y. (2018). Long-lasting geomagnetically induced currents and harmonic distortion observed in New Zealand during the 7–8 September 2017 disturbed period. *Space Weather*, 16, 704–717. <https://doi.org/10.1029/2018SW001822>
- Cohen, C. M. S., & Mewaldt, R. A. (2018). The ground-level enhancement event of September 2017 and other large solar energetic particle events of Cycle 24. *Space Weather*, 16, 1616–1623. <https://doi.org/10.1029/2018SW002006>
- Copeland, K., Matthi, D., & Meier, M. M. (2018). Solar cosmic ray dose rate assessments during GLE 72 using MIRA and PANDORA. *Space Weather*, 16, 969–976. <https://doi.org/10.1029/2018SW001917>

- Curry, S. M., Luhmann, J. G., Hara, T., Lee, C., & Jakosky, B. (2019). *Space weather events and the loss of water at Mars*. Ninth International Conference on Mars, Pasadena, California. LPI Contributions, 2089, 6357.
- Curto, J. J., Marsal, S., Blanch, E., & Altadill, D. (2018). Analysis of the solar flare effects of 6 September 2017 in the ionosphere and in the Earth's magnetic field using spherical elementary current systems. *Space Weather*, 16, 1709–1720. <https://doi.org/10.1029/2018SW001927>
- Dimmock, A. P., Rosenqvist, L., Hall, J. O., Viljanen, A., Yordanova, E., Honkonen, I., & Sj, E. C. (2019). The GIC and geomagnetic response over Fennoscandia to the 7–8 September 2017 geomagnetic storm. *Space Weather*, 17, 989–1010. <https://doi.org/10.1029/2018SW002132>
- Ehresmann, B., Hassler, D. M., Zeitlin, C., Guo, J., Wimmer-Schweingruber, R. F., Matthi, D., & Reitz, G. (2018). Energetic particle radiation environment observed by RAD on the surface of Mars during the September 2017 event. *Geophysical Research Letters*, 45, 5305–5311. <https://doi.org/10.1029/2018GL077801>
- Elrod, M. K., Bougher, S. W., Roeten, K., Sharrar, R., & Murphy, J. (2020). Structural and compositional changes in the upper atmosphere related to the PEDE-2018 dust event on Mars as observed by MAVEN NGIMS. *Geophysical Research Letters*, 47, e2019GL084378. <https://doi.org/10.1029/2019GL084378>
- Elrod, M. K., Curry, S. M., Thiemann, E. M. B., & Jain, S. K. (2018). September 2017 solar flare event: Rapid heating of the Martian neutral upper atmosphere from the X-class flare as observed by MAVEN. *Geophysical Research Letters*, 45, 8803–8810. <https://doi.org/10.1029/2018GL077729>
- Fallows, K., Withers, P., & Gonzalez, G. (2015). Response of the Mars ionosphere to solar flares: Analysis of MGS radio occultation data. *Journal of Geophysical Research: Space Physics*, 120, 9805–9825. <https://doi.org/10.1002/2015JA021108>
- Fang, X., Pawlowski, D., Ma, Y., Bougher, S., Thiemann, E., Eparvier, F., & Jakosky, B. (2019). Mars upper atmospheric responses to the 10 September 2017 solar flare: A global, time-dependent simulation. *Geophysical Research Letters*, 46, 9334–9343. <https://doi.org/10.1029/2019GL084515>
- Frissell, N. A., Vega, J. S., Markowitz, E., Gerrard, A. J., Engelke, W. D., Erickson, P. J., & Bortnik, J. (2019). High-frequency communications response to solar activity in September 2017 as observed by amateur radio networks. *Space Weather*, 17, 118–132. <https://doi.org/10.1029/2018SW002008>
- Gonzalez-Esparza, J. A., Sergeeva, M. A., Corona-Romero, P., Mejia-Ambriz, J. C., Gonzalez, L. X., De la Luz, V., & Romero-Hernandez, E. (2018). Space weather events, hurricanes, and earthquakes in Mexico in September 2017. *Space Weather*, 16, 2038–2051. <https://doi.org/10.1029/2018SW001995>
- Gurnett, D. A., Kirchner, D. L., Huff, R. L., Morgan, D. D., Persoon, A. M., Averkamp, T. F., & Picardi, G. (2005). Radar soundings of the ionosphere of Mars. *Science*, 310, 1929–1933. <https://doi.org/10.1126/science.1121868>
- Harada, Y., Gurnett, D. A., Kopf, A. J., Halekas, J. S., Ruhunusiri, S., DiBraccio, G. A., & Brain, D. A. (2018). MARSIS observations of the Martian nightside ionosphere during the September 2017 solar event. *Geophysical Research Letters*, 45, 7960–7967. <https://doi.org/10.1002/2018GL077622>
- Hassler, D. M., Zeitlin, C., Ehresmann, B., Wimmer-Schweingruber, R. F., Guo, J., Matthi, D., & Reitz, G. (2018). Space weather on the surface of Mars: Impact of the September 2017 events. *Space Weather*, 16, 1702–1708. <https://doi.org/10.1029/2018SW001959>
- Jain, S. K., Deighan, J., Schneider, N. M., Stewart, A. I. F., Evans, J. S., Thiemann, E. M. B., & Jakosky, B. M. (2018). Martian thermospheric response to an X8.2 solar flare on 10 September 2017 as seen by MAVEN/IUVS. *Geophysical Research Letters*, 45, 7312–7319. <https://doi.org/10.1029/2018GL077731>
- Jiggins, P., Clavie, C., Evans, H., O'Brien, T. P., Witasse, O., Mishev, A. L., & Nagatsuma, T. (2019). In situ data and effect correlation during September 2017 solar particle event. *Space Weather*, 17, 99–117. <https://doi.org/10.1029/2018SW001936>
- Kay, C., Airapetian, V. S., Lüftinger, T., & Kochukhov, O. (2019). Frequency of coronal mass ejection impacts with early terrestrial planets and exoplanets around active solar-like stars. *The Astrophysical Journal*, 886(2), L37. <https://doi.org/10.3847/2041-8213/ab551f>
- Kay, C., Opher, M., & Kornbleuth, M. (2016). Probability of CME impact on exoplanets orbiting M dwarfs and solar-like stars. *The Astrophysical Journal*, 826(2), 195. <https://doi.org/10.3847/0004-637X/826/2/195>
- Kong, X., Li, G., & Chen, Y. (2013). A statistical study of the spectral hardening of continuum emission in solar flares. *Astrophysical Journal*, 774, 140. <https://doi.org/10.1088/0004-637X/774/2/140>
- Krasnopolsky, V. A. (2002). Mars' upper atmosphere and ionosphere at low, medium, and high solar activities: Implications for evolution of water. *Journal of Geophysical Research*, 107(E12), 5128. <https://doi.org/10.1029/2001JE001809>
- Lee, Y., Dong, C., Pawlowski, D., Thiemann, E., Tennishev, V., Mahaffy, P., & Eparvier, F. (2018). Effects of a solar flare on the Martian hot O corona and photochemical escape. *Geophysical Research Letters*, 45, 6814–6822. <https://doi.org/10.1029/2018GL077732>
- Lee, Y., Fang, X., Gacesa, M., Ma, Y., Tennishev, V., Mahaffy, P., & Jakosky, B. (2020). Effects of global and regional dust storms on the Martian hot O corona and photochemical loss. *Journal of Geophysical Research: Space Physics*, 125, e2019JA027115. <https://doi.org/10.1029/2019JA027115>
- Lee, C. O., Jakosky, B. M., Luhmann, J. G., Brain, D. A., Mays, M. L., Hassler, D. M., & Halekas, J. S. (2018). Observations and impacts of the 10 September 2017 solar events at Mars: An overview and synthesis of the initial results. *Geophysical Research Letters*, 45, 8871–8885. <https://doi.org/10.1029/2018GL079162>
- Lillis, R. J., Brain, D. A., Bougher, S. W., Leblanc, F., Luhmann, J. G., Jakosky, B. M., & Lin, R. P. (2015). Characterizing atmospheric escape from Mars today and through time, with MAVEN. *Space Science Reviews*, 195(1–4), 357–422. <https://doi.org/10.1007/s12124-015-0165-8>
- Linty, N., Minetto, A., Dovis, F., & Spogli, L. (2018). Effects of phase scintillation on the GNSS positioning error during the September 2017 storm at Svalbard. *Space Weather*, 16, 1317–1329. <https://doi.org/10.1029/2018SW001940>
- Liu, G., England, S. L., Lillis, R. J., Withers, P., Mahaffy, P. R., Rowland, D. E., & Jakosky, B. (2018). Thermospheric expansion associated with dust increase in the lower atmosphere on Mars observed by MAVEN/NGIMS. *Geophysical Research Letters*, 45, 2901–2910. <https://doi.org/10.1002/2018GL077525>
- Luhmann, J. G., Mays, M. L., Li, Y., Lee, C. O., Bain, H., Odstrcil, D., & Petrie, G. (2018). Shock connectivity and the late cycle 24 solar energetic particle events in July and September 2017. *Space Weather*, 16, 557–568. <https://doi.org/10.1029/2018SW001860>
- Ma, Y., Fang, X., Halekas, J. S., Xu, S., Russell, C. T., Luhmann, J. G., & Jakosky, B. M. (2018). The impact and solar wind proxy of the 2017 September ICME event at Mars. *Geophysical Research Letters*, 45, 7248–7256. <https://doi.org/10.1029/2018GL077707>
- Mahaffy, P. R., Benna, M., Elrod, M., Yelle, R. V., Bougher, S. W., Stone, S. W., & Jakosky, B. M. (2015). Structure and composition of the neutral upper atmosphere of Mars from the MAVEN NGIMS investigation. *Geophysical Research Letters*, 42, 8951–8957. <https://doi.org/10.1002/2015GL065329>

- Mahaffy, P. R., Benna, M., King, T., Harpold, D. N., Arvey, R., Barciniak, M., & Nolan, J. T. (2015). The Neutral Gas and Ion Mass Spectrometer on the Mars Atmosphere and Volatile Evolution mission. *Space Science Reviews*, 195, 49–73. <https://doi.org/10.1007/s11214-014-0091-1>
- Mahajan, K. K., Lodhi, N. K., & Singh, S. (2009). Ionospheric effects of solar flares at Mars. *Geophysical Research Letters*, 36, L15207. <https://doi.org/10.1029/2009GL039454>
- Matthiä, D., Meier, M. M., & Berger, T. (2018). The solar particle event on 10–13 September 2017: Spectral reconstruction and calculation of the radiation exposure in aviation and space. *Space Weather*, 16, 977–986. <https://doi.org/10.1029/2018SW001921>
- Mavromichalaki, H., Gerontidou, M., Paschalis, P., Paouris, E., Tezari, A., Sgouropoulos, C., & Dierckx, M. (2018). Real-time detection of the ground level enhancement on 10 September 2017 by A.Ne.Mo.S.: System report. *Space Weather*, 16, 1797–1805. <https://doi.org/10.1029/2018SW001992>
- Mayyasi, M., Bhattacharyya, D., Clarke, J., Catalano, A., Benna, M., Mahaffy, P., & Jakosky, B. (2018). Significant space weather impact on the escape of hydrogen from Mars. *Geophysical Research Letters*, 45, 8844–8852. <https://doi.org/10.1029/2018GL077727>
- Mendillo, M., Erickson, P. J., Zhang, S. R., Mayyasi, M., Narvaez, C., Thiemann, E., & Peterson, W. (2018). Flares at Earth and Mars: An ionospheric escape mechanism? *Space Weather*, 16, 1042–1056. <https://doi.org/10.1029/2018SW001872>
- Mendillo, M., Withers, P., Hinson, D., Rishbeth, H., & Reinisch, B. (2006). Effects of solar flares on the ionosphere of Mars. *Science*, 311, 1135–1138. <https://doi.org/10.1126/science.1122099>
- Mishev, A. L., & Usoskin, I. G. (2018). Assessment of the radiation environment at commercial jet-flight altitudes during GLE 72 on 10 September 2017 using neutron monitor data. *Space Weather*, 16, 1921–1929. <https://doi.org/10.1029/2018SW001946>
- Moore, C. S., Chamberlin, P. C., & Hock, R. (2014). Measurements and modeling of total solar irradiance in X-class solar flares. *Astrophysical Journal*, 787, 32. <https://doi.org/10.1088/0004-637X/787/1/32>
- Nier, A. O., & McElroy, M. B. (1977). Composition and structure of Mars' upper atmosphere: Results from the neutral mass spectrometers on Viking 1 and 2. *Journal of Geophysical Research*, 82, 4341–4349. <https://doi.org/10.1029/J082i028p04341>
- O'Brien, T. P., Mazur, J. E., & Looper, M. D. (2018). Solar energetic proton access to the magnetosphere during the 10–14 September 2017 particle event. *Space Weather*, 16, 2022–2037. <https://doi.org/10.1029/2018SW001960>
- Obana, Y., Maruyama, N., Shinbori, A., Hashimoto, K. K., Fedrizzi, M., Nos, M., & Shinohara, I. (2019). Response of the ionosphere-plasmasphere coupling to the September 2017 storm: What erodes the plasmasphere so severely? *Space Weather*, 17, 861–876. <https://doi.org/10.1029/2019SW002168>
- Pawlowski, D. J., & Ridley, A. J. (2008). Modeling the thermospheric response to solar flares. *Journal of Geophysical Research*, 113, A10309. <https://doi.org/10.1029/2008JA013182>
- Piersanti, M., Di Matteo, S., Carter, B. A., Currie, J., & D'Angelo, G. (2019). Geoelectric field evaluation during the September 2017 geomagnetic storm: MA.I.GIC. model. *Space Weather*, 17, 1241–1256. <https://doi.org/10.1029/2019SW002202>
- Ramstad, R., Holmström, M., Futaana, Y., Lee, C. O., Rahmati, A., Dunn, P., & Larson, D. (2018). The September 2017 SEP event in context with the current solar cycle: Mars Express ASPERA-3/IMA and MAVEN/SEP observations. *Geophysical Research Letters*, 45, 7306–7311. <https://doi.org/10.1029/2018GL077842>
- Redmon, R. J., Seaton, D. B., Steenburgh, R., He, J., & Rodriguez, J. V. (2018). September 2017's geoeffective space weather and impacts to Caribbean radio communications during hurricane response. *Space Weather*, 16, 1190–1201. <https://doi.org/10.1029/2018SW001897>
- Ribas, I., Guinan, E. F., Güdel, M., & Audard, M. (2005). Evolution of the solar activity over time and effects on planetary atmospheres. I. High-energy irradiances (1–1700 Å). *The Astrophysical Journal*, 622(1), 680–694. <https://doi.org/10.1086/427977>
- Roeten, K. J., Bougher, S. W., Benna, M., Mahaffy, P. R., Lee, Y., Pawlowski, D., & López-Valverde, M. A. (2019). MAVEN/NGIMS thermospheric neutral wind observations: Interpretation using the M-GITM general circulation model. *Journal of Geophysical Research: Planets*, 124, 3283–3303. <https://doi.org/10.1029/2019JE005957>
- Sánchez-Cano, B., Blelly, P. L., Lester, M., Witasse, O., Cartacci, M., Orosei, R., & Kopf, A. J. (2019). Origin of the extended Mars radar blackout of September 2017. *Journal of Geophysical Research: Space Physics*, 124, 4556–4568. <https://doi.org/10.1029/2018JA026403>
- Schillings, A., Nilsson, H., Slapak, R., Wintoft, P., Yamauchi, M., Wik, M., & Carr, C. M. (2018). O⁺ escape during the extreme space weather event of 4–10 September 2017. *Space Weather*, 16, 1363–1376. <https://doi.org/10.1029/2018SW001881>
- Schneider, N. M., Jain, S. K., Deighan, J., Nasr, C. R., Brain, D. A., Larson, D., & Jakosky, B. M. (2018). Global aurora on Mars during the September 2017 space weather event. *Geophysical Research Letters*, 45, 7391–7398. <https://doi.org/10.1029/2018GL077772>
- Schrijver, C. J., & Siscoe, G. L. (2010). *Heliophysics*. Cambridge: Cambridge University Press.
- Schwadron, N. A., Rahmanifard, F., Wilson, J., Jordan, A. P., Spence, H. E., Joyce, C. J., & Zeitlin, C. (2018). Update on the worsening particle radiation environment observed by crater and implications for future human deep-space exploration. *Space Weather*, 16, 289–303. <https://doi.org/10.1002/2017SW001803>
- Siskind, D. E., & Bougher, S. W. (2016). Aeronomy of terrestrial upper atmospheres. In C. J. Schrijver, F. Bagenal, J. J. Sojka (Eds.), *Heliophysics: Active stars, their astrospheres, and impacts on planetary environments* (pp. 201–225). Cambridge: Cambridge Univ. Press. <https://doi.org/10.1017/CBO9781316106778.010>
- Slipski, M., Jakosky, B. M., Benna, M., Elrod, M., Mahaffy, P., Kass, D., & Yelle, R. (2018). Variability of Martian turbopause altitudes. *Journal of Geophysical Research: Planets*, 123, 2939–2957. <https://doi.org/10.1029/2018JE005704>
- Strobel, D. F. (2002). Aeronomic systems on planets, moons, and comets. In M. Mendillo, A. Nagy & J. Waite (Eds.), *Atmospheres in the solar system: Comparative aeronomy* (pp. 7–22). Washington, DC: American Geophysical Union.
- Thiemann, E. M. B., Andersson, L., Lillis, R., Withers, P., Xu, S., Elrod, M., & Deighan, J. (2018). The Mars topside ionosphere response to the X8.2 solar flare of 10 September 2017. *Geophysical Research Letters*, 45, 8005–8013. <https://doi.org/10.1029/2018GL077730>
- Thiemann, E. M. B., Eparvier, F. G., Andersson, L. A., Fowler, C. M., Peterson, W. K., Mahaffy, P. R., & Jakosky, B. M. (2015). Neutral density response to solar flares at Mars. *Geophysical Research Letters*, 42, 8986–8992. <https://doi.org/10.1002/2015GL066334>
- Tsurutani, B. T., Verkhoglyadova, O. P., Mannucci, A. J., Lakhina, G. S., Li, G., & Zank, G. P. (2009). A brief review of “solar flare effects” on the ionosphere. *Radio Science*, 44, RS0A17. <https://doi.org/10.1029/2008RS004029>
- Withers, P. (2009). A review of observed variability in the dayside ionosphere of Mars. *Advances in Space Research*, 44, 277–307. <https://doi.org/10.1016/j.asr.2009.04.027>
- Withers, P., & Pratt, R. (2013). An observational study of the response of the upper atmosphere of Mars to lower atmospheric dust storms. *Icarus*, 225(1), 378–389. <https://doi.org/10.1016/j.icarus.2013.02.032>
- Xu, S., Fang, X., Mitchell, D. L., Ma, Y., Luhmann, J. G., DiBraccio, G. A., & Lee, C. O. (2018). Investigation of Martian magnetic topology response to 2017 September ICME. *Geophysical Research Letters*, 45, 7337–7346. <https://doi.org/10.1029/2018GL077708>

- Xu, S., Thiemann, E., Mitchell, D., Eparvier, F., Pawlowski, D., Benna, M., & Mazelle, C. (2018). Observations and modeling of the Mars low-altitude ionospheric response to the 10 September 2017 X-class solar flare. *Geophysical Research Letters*, *45*, 7382–7390. <https://doi.org/10.1029/2018GL078524>
- Yamauchi, M., Sergienko, T., Enell, C. F., Schillings, A., Slapak, R., Johnsen, M. G., & Nilsson, H. (2018). Ionospheric response observed by EISCAT during the 6–8 September 2017 space weather event: Overview. *Space Weather*, *16*, 1437–1450. <https://doi.org/10.1029/2018SW001937>
- Yasyukevich, Y., Astafyeva, E., Padokhin, A., Ivanova, V., Syrovatskii, S., & Podlesnyi, A. (2018). The 6 September 2017 X-class solar flares and their impacts on the ionosphere, GNSS, and HF radio wave propagation. *Space Weather*, *16*, 1013–1027. <https://doi.org/10.1029/2018SW001932>
- Zeitlin, C., Hassler, D. M., Guo, J., Ehresmann, B., Wimmer-Schweingruber, R. F., Rafkin, S. C. R., & Reitz, G. (2018). Analysis of the radiation hazard observed by RAD on the surface of Mars during the September 2017 solar particle event. *Geophysical Research Letters*, *45*, 5845–5851. <https://doi.org/10.1029/2018GL077760>
- Zurek, R. W., Tolson, R. A., Bougher, S. W., Lugo, R. A., Baird, D. T., Bell, J. M., & Jakosky, B. M. (2017). Mars thermosphere as seen in MAVEN accelerometer data. *Journal of Geophysical Research: Space Physics*, *122*, 3798–3814. <https://doi.org/10.1002/2016JA023641>